

# Supplementary Material for “Tailored nanophononic wavefield in a patterned bilayer system probed by ultrafast convergent beam electron diffraction”

N. Bach,<sup>1</sup> A. Feist,<sup>2</sup> M. Möller,<sup>2</sup> C. Ropers,<sup>2</sup> and S. Schäfer<sup>1, a)</sup>

<sup>1)</sup>*Institute of Physics, University of Oldenburg, 26129 Oldenburg, Germany*

<sup>2)</sup>*Max Planck Institute for Multidisciplinary Sciences, 37077 Göttingen, Germany*

## S1. SAMPLE SYSTEM

The sample is based on a single-crystalline, 35-nm thin silicon membrane (Plano GmbH) (approximate dimension:  $100 \times 100 \mu\text{m}^2$ ) on which a single 2- $\mu\text{m}$  wide platinum stripe is fabricated using electron beam lithography and a thermal evaporation process. The stripe is centered within the membrane and has a length of 100  $\mu\text{m}$ , a film thickness of 10 nm and an edge sharpness of approximately 10 nm. A 1-nm thin chromium adhesion layer deposited between the membrane and the platinum layer is neglected in the analysis of laser-induced structural dynamics. The long side of the Pt stripe is orientated along the  $[\bar{1}10]$ -direction of the silicon membrane [see Fig. 1(a)].

## S2. ULTRAFAST TRANSMISSION ELECTRON MICROSCOPE IN CBED MODE

All experimental data were acquired with the Göttingen Ultrafast Transmission Electron Microscope (UTEM), based on a JEOL JEM-2100F Schottky field emission electron microscope. The instrument is modified to allow for ultrashort electron pulse generation from a ZrO/W Schottky field emitter tip using 400-nm ultrashort laser pulses yielding low-emittance electron pulses with down to 200-fs duration.<sup>1</sup> The laser-driven electron gun was operated at an acceleration potential of 120 kV. For laser-pump/electron-probe experiments, the sample is illuminated by p-polarized 800-nm optical pump pulses with 1-ps pulse duration at a 250-kHz repetition rate and an incidence angle of  $55^\circ$  relative to the electron beam. The optical beam is focused down to 50  $\mu\text{m}$  full-width-at-half-maximum (FWHM). Diffraction patterns for the ultrafast convergent beam electron diffraction (U-CBED) experiment were recorded with a focused electron beam with a full convergence angle of 32 mrad (condenser lens aperture 200- $\mu\text{m}$  diameter). The minimal focal spot for these TEM settings was about 15 nm. For the effective electron spot diameters during the U-CBED experiment, additional contributions such as beam defocussing, and sample and beam drifts need to be considered. The specimen was mounted in a JEOL double-tilt holder, which was rotated by about  $-34^\circ$  around the holder axis (i.e., laboratory-fixed  $X$ -axis) and  $3^\circ$  around the rotated  $Y$ -axis. All diffraction patterns were recorded on a charge-coupled device camera (Gatan UltraScan 4000), binned to  $1024 \times 1024$  pixels (0.164 mrad per pixel angular resolution)

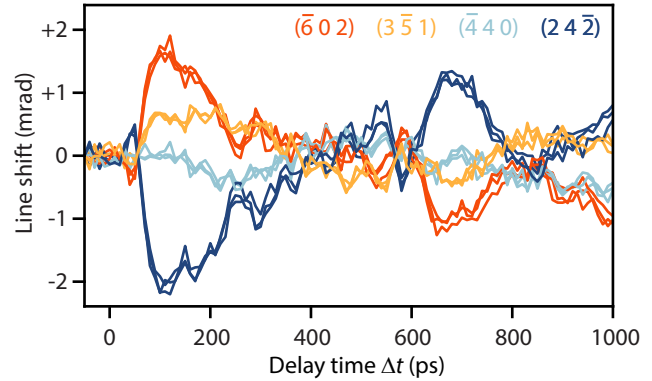


FIG. S1. Delay-dependent angular shifts of exemplary Bragg lines shown for three repetitions of 1000-ps long delay scans (typical measurement time of each scan about 2 h). Both, the overall behavior and small-amplitude high-frequency oscillations are well reproduced across the different delay scans.

with an indicated projection camera length of 25 cm. Images are acquired with 60-s exposure time and  $4 \times 4$  binning in 2 or 10 ps time steps for the 160-ps long and 1000-ps long delay scan, respectively. Similar probe positions in a distance of approximately 170 nm from the long platinum edge are chosen in both delay scans.

## S3. EXTRACTION OF BRAGG-SCATTERED LINE PROFILES

For the analysis of the Bragg-scattered line profiles in the ultrafast convergent beam electron diffraction experiments, each single diffraction image is centered with respect to the central disk. Rectangular regions of interest (ROI) around the Bragg lines with one edge parallel to the respective Bragg line are defined. Afterwards, the scattered intensity across the full Bragg line, the line position, and spatial width are extracted from each ROI using a Lorentzian fit that includes a linear offset. The linear background is subtracted from the experimental Bragg-scattered line profiles. Fluctuations in the electron beam current over time are compensated by normalization to the spatially integrated intensity in the central disk of each diffractogram. Although we only present the results of a single measurement, the Bragg line shifts were highly reproducible, as shown in Fig. S1. No averaging over scans is performed in the data analysis.

<sup>a)</sup>sascha.schaefer@uni-oldenburg.de

#### S4. CONVERGENT BEAM ELECTRON DIFFRACTION PATTERN

The positions and inclination angles of deficit and excess Bragg lines in a diffraction pattern obtained with a convergent electron beam are linked to the size, shape, and orientation of the local crystal unit cell at the electron probing position. The real-space basis  $B_u^{\text{sample}} = (a_1 \ a_2 \ a_3)$  of the silicon unit cell in the sample-fixed coordinate system ( $x$ ,  $y$ , and  $z$ ) [cf. Fig. 1(a)] is defined by unit vectors  $a_1 = \frac{a_{\text{Si}}}{\sqrt{2}} (1 \ 1 \ 0)^T$ ,  $a_2 = \frac{a_{\text{Si}}}{\sqrt{2}} (1 \ -1 \ 0)^T$ , and  $a_3 = a_{\text{Si}} (0 \ 0 \ 1)^T$  with the silicon lattice constant  $a_{\text{Si}} = 5.43 \text{ \AA}$ .<sup>2</sup> To account for a tilted sample orientation, a rotation matrix  $R = R_X(\alpha) \cdot R_Y(\beta) \cdot R_Z(\gamma)$  is applied that is constructed from individual matrices  $R_X$ ,  $R_Y$ , and  $R_Z$  corresponding to rotations around the laboratory-fixed  $X$ ,  $Y$ , and  $Z$  coordinate axes.<sup>†</sup> For the orientation of the coordinate system relative to the microscope column, see Fig. 1(a). The rotated real-space unit cell basis in the laboratory-fixed coordinate system is given by  $B_u^{\text{lab}} = R B_u^{\text{sample}}$ . The reciprocal basis  $G_u^{\text{lab}}$  is obtained from the identity  $G_u^{\text{lab}} B_u^{\text{lab}} = \mathbb{1}$  (in the  $1/\lambda$ -convention). Reciprocal lattice vectors  $G$  with Miller indices  $h$ ,  $k$ , and  $l$  are consequently expressed as  $G = G_u(hkl)^T$ . Bragg diffraction<sup>3</sup> is observed if the incident and scattered electron wavevectors  $k_0$  and  $k$  differ by a reciprocal lattice vector of the diffracting crystal, i.e.,  $G = k - k_0$ . Employing elastic scattering and assuming small scattering angles, the expression  $-G^2/2 = k_0 G = k_{0,X} G_X + k_{0,Y} G_Y + k_{0,Z} G_Z$  between the components of  $k_0$  and  $G$  is obtained. Applying  $k_{0,X}$ ,  $k_{0,Y} \ll k_0$  and  $k_X, k_Y \ll k$  (paraxial approximation for the optical axis oriented along  $Z$ ), the scattering condition can be linearized, yielding

$$-\frac{G^2}{2} = k_X G_X + k_Y G_Y + k_0 G_Z \quad (\text{S4.1})$$

with  $G^2 = G_X^2 + G_Y^2 + G_Z^2$ .  $[k_X, k_Y]$  describe straight lines in the transverse  $k$ -space for each  $G$ , along which incident electron intensity is scattered out to larger angles. The resulting excess Bragg lines have a distance

$$r_G = \frac{-G^2/2 + k_0 G_Z}{\sqrt{G_X^2 + G_Y^2}} + \sqrt{G_X^2 + G_Y^2} \quad (\text{S4.2})$$

from the center of the diffraction pattern. Angular line shifts are retrieved by division of Eq. (S4.2) with the wavenumber  $k_0$  of the incident electron beam.

In the present work, we quantify the optically induced structural distortion of the silicon membrane by a deformation gradient tensor  $F$  with spatiotemporal dependency.<sup>4</sup> Within linear elasticity theory, the application of  $F(\Delta t) = \varepsilon(\Delta t) +$

$\omega(\Delta t) + \mathbb{1}$ , where  $\varepsilon$  and  $\omega$  are the symmetric shear and anti-symmetric rotation tensors, respectively, leads to a deformed unit cell basis of the form  $B_F^{\text{lab}} = R \cdot F^{\text{sample}} \cdot B_u^{\text{sample}}$  and a new reciprocal lattice basis  $G_F^{\text{lab}} = (B_F^{\text{lab}})^{-1}$ . The tensors are a function of the displacement gradients of the displacement vector  $u$  along the coordinate axes. In linear approximation, we write:

$$\varepsilon_{ij} = \frac{1}{2} \left( \frac{\partial u_i}{\partial x_j} + \frac{\partial u_j}{\partial x_i} \right), \quad \omega_{ij} = \frac{1}{2} \left( \frac{\partial u_i}{\partial x_j} - \frac{\partial u_j}{\partial x_i} \right),$$

with  $i, j \in (x, y, z)$ .

#### S5. LINE SENSITIVITY TO SPECIFIC TENSOR COMPONENTS AND RECIPROCAL LATTICE VECTOR COMPONENTS

Generally, the Bragg line positions  $r_G$  depend nonlinearly on the reciprocal lattice vector and tensor components. Assuming only small tensor components  $F_{ij} = \delta_{ij} + \Delta F_{ij}$ , where  $\delta_{ij}$  is the Kronecker delta and  $\Delta F_{ij}$  is a small number in each tensor component separately, the relation can be linearized in the form

$$\Delta r_G = \sum_{i,j} \frac{\partial r_G}{\partial F_{ij}} \Delta F_{ij}. \quad (\text{S5.3})$$

The difference quotients  $\frac{\partial r_G}{\partial F_{ij}}$  can be computed either analytically or approximated numerically. The results  $\frac{\partial r_G}{\partial F_{ij}}$  for  $n$  selected Bragg lines and  $m$  tensor components can be aggregated in a  $n \times m$  matrix  $A$ . Inserting numerically calculated tensor components (cf. supplementary material S7) in Eq. (S5.3), the time-dependent shift of selected Bragg lines can be predicted, as shown in Fig. 3(c).

Extracting, in turn, the time-dependent displacement gradient tensor  $F$  from the experimentally observed angular Bragg line shifts would require matrix  $A$  to have a numerically stable inverse. However, it is found that even small variations in the line shift on the order of 0.05 mrad already have a strong impact on the retrieved tensor, indicating that a full reconstruction of the tensor  $F$  from the experimental line shifts is not possible based on diffraction data recorded for a single sample orientation. To construct the tensor component subspace which the experiment is still sensitive to, we perform a singular value decomposition  $A = U \cdot S \cdot V^T$  of the matrix  $A$ , with unitary matrices  $U$  and  $V$ , and the diagonal matrix  $S$  (see supplemental source code for numerical results).  $V$  contains a set of  $m$  basis vectors of the tensor component vector space, which by the action of  $A$  are stretched by a factor  $S_{mm}$ . Thereby, basis vectors with small  $S_{mm}$  do not result in an appreciable Bragg line shift and cannot be accurately reconstructed from the experimental line shift. Considering an experimental accuracy of the recorded shifts of about  $\Delta r_{\text{min}} = 0.05 \text{ mrad}$ , only two basis vectors in  $V$  correspond to distortions for which the experiment yields a sensitivity of better than  $r_{\text{min}}/S_{11,22} < 10^{-5}$ . For a third vector, a sensitivity of about  $6.4 \times 10^{-4}$  is found, and worse than  $3.1 \times 10^{-3}$  for

<sup>†</sup>The sample orientation is retrieved from a comparison between recorded and simulated diffraction patterns as follows:

160 ps delay scan:  $\alpha = 25.09^\circ$ ,  $\beta = -0.30^\circ$  and  $\gamma = -4.66^\circ$ ;  
1000 ps delay scan:  $\alpha = 25.18^\circ$ ,  $\beta = -0.63^\circ$  and  $\gamma = -5.41^\circ$ .

all other basis vectors. For a comparison of these tensor sensitivities to the magnitude of the expected tensor components, see Fig. 3(a).

An intuitive interpretation of the basis vectors, to which the experiment is most sensitive, is gained by transforming the calculated base vectors in  $V$  into the laboratory coordinate system, using the rotation matrix  $R$ . It is observed that line shifts are predominantly governed by the gradient displacement components  $F_{XZ}$ ,  $F_{YZ}$ , and, to a lesser extent, also by  $F_{ZZ}$ . These tensor components  $F_{iZ} = \delta_{iZ} + \frac{\partial u_i}{\partial Z}$  correspond to changes in the displacement vector along the  $Z$ -axis, i.e., parallel to the electron beam.

A general picture on the sensitivity of line shifts in UCBED is obtained by considering their response to changes in the reciprocal lattice vectors:

$$\Delta r = \sum_{i=X,Y,Z} \frac{\partial r}{\partial G_i} \Delta G_i. \quad (\text{S5.4})$$

Here,  $\Delta G_i = G_{i,F} - G_{i,0}$  is the difference of the reciprocal lattice vector component  $i$  after and before the application of the deformation gradient tensor  $F$ . From Eq. (S4.2) for the excess Bragg line positions, the following partial derivatives are obtained:

$$\begin{aligned} \frac{\partial r}{\partial G_X} &= \frac{(G^2/2 - k_0 G_Z) \cdot G_X}{(G_X^2 + G_Y^2)^{3/2}} \\ \frac{\partial r}{\partial G_Y} &= \frac{(G^2/2 - k_0 G_Z) \cdot G_Y}{(G_X^2 + G_Y^2)^{3/2}} \\ \frac{\partial r}{\partial G_Z} &= \frac{-G_Z + k_0}{\sqrt{G_X^2 + G_Y^2}}. \end{aligned} \quad (\text{S5.5})$$

Since  $(G^2/2) \approx k_0 G_Z$ ,  $\frac{\partial r}{\partial G_{X,Y}}$  can be neglected and line shifts  $\Delta r$  are dominated by  $\partial r / \partial G_Z$ .

Due to the deformation given by  $F$ , the reciprocal basis matrix  $G_u^{\text{lab}}$  changes to  $G_F^{\text{lab}} = G_u^{\text{lab}} (F^{\text{lab}})^{-1}$ . Therefore,  $\Delta G_Z$  is only influenced by the last column of  $F^{\text{lab}}$ , which may contain a dilatational component along the  $Z$ -direction ( $F_{ZZ}$ ) or shear-rotational components perpendicular to the  $Z$ -axis ( $F_{XZ}$  and  $F_{YZ}$ ). For the case of static residual strains in heterogeneous materials, it was demonstrated that an unambiguous tensor measurement can be obtained by CBED tomography using three independent projection axes.<sup>5</sup>

## S6. THEORETICAL DESCRIPTION OF BRAGG LINE PROFILES

Considering only single scattering events (kinematical approximation) and a monochromatic, spatially coherent incident electron wave, the wavefield  $\hat{\psi}(k)$  after sample interaction can be approximated by a superposition of wave components with wavevectors  $k$ , each with an amplitude proportional to  $f(\Delta k) = \pi \int d^3 r e^{-2\pi i \Delta k r} \rho(r)$ .<sup>4</sup> Here,  $\rho(r)$  is the interaction potential experienced by the electron when transversing the

crystal, and  $\Delta k = k - k_0$  is the momentum change between the incident and the scattered electron wave.

For a perfect crystal, the potential  $\rho(r)$  is given by the product of a function describing the infinite lattice  $l(r)$  and a shape function  $s(r)$  which defines the shape and extent of the nanocrystal (e.g., the finite Si membrane thickness):  $\rho(r) = s(r)l(r)$ . Local displacements  $u(r)$ , arising for example from propagating Lamb waves, change the lattice function into  $l(r + u(r))$  such that  $f(\Delta k)$  in the vicinity of reciprocal lattice vectors  $k \approx G$  is modulated by an additional phase factor  $\exp[i\phi]$  containing the projection of the displacement field onto  $G$ .<sup>6</sup> The strained crystal therefore imprints a phase modulation on the electron exit wave, resulting in diffracted intensities  $I(\Delta k - G) \propto |\mathcal{F}(\exp[iG \cdot u(r)])|^2$ .

## S7. NUMERICAL SIMULATION OF STRUCTURAL DYNAMICS IN PT-STRIPE/SI-MEMBRANE HETEROSTRUCTURE

To obtain a better understanding of the spatiotemporal acoustic wave propagation, we numerically solve the two-dimensional elastodynamic wave equation using finite-element simulations in COMSOL Multiphysics.<sup>7</sup> For the sample geometry, we consider an infinitely extending Pt-stripe on a Si-membrane imposing a plane strain ansatz and a mirror symmetry plane ( $xz$ -plane) along the platinum stripe. The membrane and stripe thickness and stripe width are adopted according to the experimental dimensions. The presence of the nominally 1-nm thin chromium adhesion layer is neglected. In order to reduce computation time, the silicon membrane is truncated  $6\mu\text{m}$  away from platinum stripe instead of  $100\mu\text{m}$ . For the given sound velocities and the chosen geometry dimensions, no acoustic wave reflections from the simulation box boundaries are expected within the first nanosecond.

Since acoustic sound velocities in silicon depend on the wave propagation direction, we employ a symmetry-adapted stiffness tensor. Specifically, the rotated stiffness tensor  $C_{\text{rot}}$  in Voigt-notation (with the  $x$  and  $y$  coordinates pointing along the  $[110]$ - and  $[\bar{1}10]$ -directions) is obtained from the conventional stiffness tensor by a basis change  $C_{\text{rot}} = K \cdot C \cdot K^T$ . For silicon, the standard components in  $C$  are  $C_{11} = 166\text{ GPa}$ ,  $C_{12} = 64\text{ GPa}$ ,  $C_{44} = 80\text{ GPa}$ .<sup>2,8</sup> For the definition of  $K$ , see Ref. (9). For platinum, isotropic elasticity properties<sup>2</sup> are assumed, governed by Young's modulus  $E = 168\text{ GPa}$ , Poisson's ratio  $\nu = 0.38$  and mass density  $\rho = 21\,450\text{ kg m}^{-3}$ .

The simulation is carried out using a combination of the COMSOL "Solid State" and "Heat Transfer in Solids" modules to solve for the time-dependent heat transfer and structural dynamics in the heterogeneous system. The absorbed laser power per unit volume at a pump wavelength of  $800\text{ nm}$  is modeled as a depth- and time-dependent heat source  $Q$  in the platinum layer. The parameters of the heat source are defined by the optical absorption coefficient of platinum<sup>10</sup> ( $a_c = 1.2688 \times 10^6\text{ cm}^{-1}$ ), the optical reflectivity ( $R_{\text{Pt}} = 0.97$ , p-polarized) at the employed wavelength and incidence angle, a laser fluence of  $8.5\text{ mJ cm}^{-2}$  estimated from experimental parameters, and considering a laser pulse duration of

100 fs (FWHM). The thermal coupling between the two media is defined by the Kapitza thermal boundary resistance<sup>11</sup>  $R_{\text{th}} = 1.1 \times 10^{-8} \text{ m}^2 \text{ KW}^{-1}$ . For the adopted thermal resistance, the initial temperature difference between platinum and silicon in the bilayer region drops to 10 % after about 500 ps. During the simulation time of 1 ns, a substantial lateral temperature gradient persists within the silicon membrane. For matching the amplitude of the simulated structural dynamics with the experimental data, the displacement field was scaled by a factor of 5.4 (cf. Fig. S2). This scaling factor may account for an increased absorbed energy in the bilayer system due to optical interferences not included in the numerical simulation. The scaled maximum temperature increase of about 300 K as obtained in the simulation is in reasonable agreement with the temperature change extracted from the Debye Waller analysis (cf. supplementary material S9). Additional effects such as the detailed mechanical coupling of the two material layers and a potential (non-)thermal hot electron distribution in the silicon membrane are expected to affect the time-dependent distortion to some extent but are not considered in detail here.

Experimentally, it was found that the silicon membrane in the vicinity to the platinum stripe is bent by about  $5^\circ$  due to the preparation process. Including a corresponding initial stress distribution in the structural dynamics simulation did not substantially influence the predicted Bragg line shifts.

The numerically obtained strain field can be decomposed into a superposition of propagating waves by performing a spatial and temporal Fast Fourier transform (FFT) of the simulated displacement field. Specifically, the mean value of the displacement components  $u_x$  and  $u_z$  along the  $z$ -axis is calculated for the first 1000 nm next to the platinum stripe and the first 400 ps after optical excitation. For evaluating the Fourier transform, the obtained spatiotemporal displacement maps are smoothed by a supergaussian window centered at a distance of 500 nm and a temporal delay of 200 ps. The signal of the individual FFTs is normalized to the maximum amplitude found in localized high-frequency resonances, yielding the results shown in Figs. 4(b) and 4(c).

## S8. ACOUSTIC LAMB WAVE DESCRIPTION FOR ANISOTROPIC SILICON

To derive the dispersion of acoustic waves in a crystalline thin film, the elastodynamic equation of motion with traction free mechanical boundary conditions at the membrane surfaces needs to be solved.<sup>12,13</sup> For single-layer isotropic media or high symmetry directions in anisotropic materials (as in the chosen silicon membrane), the solutions of this guided wave problem are so-called Lamb waves<sup>14,15</sup> which are superpositions of quasi-longitudinal and -transverse bulk waves and are classified as symmetric (S), antisymmetric (A), and shear-horizontal (SH) waves. Symmetric Lamb waves are also termed dilatational waves, and antisymmetric waves flexural waves, due to their overall impact on the membrane deformation.

The corresponding dispersion relations for the generally in-

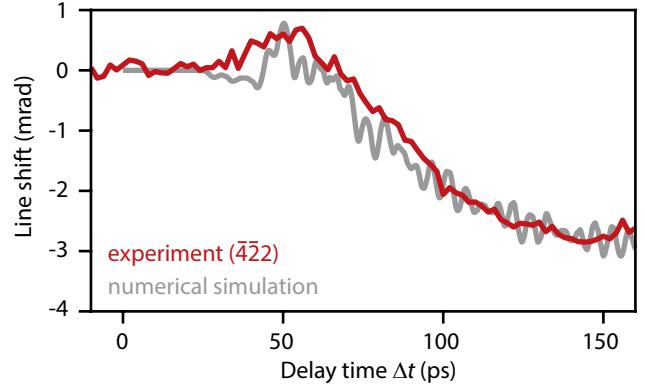


FIG. S2. Determining scaling factor of the numerical results. For matching the experimental Bragg line shifts, the calculated displacement fields are scaled by a factor of 5.4. A comparison between experimental and scaled calculated results is shown for the (422) Bragg line shift.

finite number of symmetric and antisymmetric modes are in the isotropic case given by an explicit characteristic function called Rayleigh-Lamb equation:<sup>12,13</sup>

$$\frac{\tan(hk_z^l + \alpha)}{\tan(hk_z^t + \alpha)} = \frac{k_z^t}{k_z^l} \left( 1 - \frac{\omega^4}{4k^2 (k_z^t)^2 \cdot v_t^4} \right), \quad (\text{S8.6})$$

with parameters

$$\left(k_z^l\right)^2 = \frac{\omega^2}{v_l^2} - k^2 \quad \text{and} \quad \left(k_z^t\right)^2 = \frac{\omega^2}{v_t^2} - k^2. \quad (\text{S8.7})$$

Here,  $k_z^l$  and  $k_z^t$  are the out-of-plane wavevector components for longitudinal and transverse acoustic waves given for an angular wave frequency  $\omega = 2\pi f$ , in-plane wave vector  $k$ , and acoustic sound velocities  $v_l$  and  $v_t$ . The sample thickness  $d$  is included in variable  $h = d/2$ . Symmetric and antisymmetric modes are separated by choosing  $\alpha = 0$  and  $\alpha = \pi/2$ , respectively. Since no analytic expression for the various branches of the dispersion curve exists, numerical root-finding algorithms need to be implemented to solve for the Lamb in-plane wavenumber at a given frequency.

For anisotropic materials, however, the quasi-longitudinal and -transverse bulk sound velocities depend on the propagation direction. Similar expressions as the Rayleigh-Lamb wave dispersion equations for isotropic media are in particular obtained for mode propagation in symmetry directions:<sup>16</sup>

$$\frac{\tan(hk_z^l)}{\tan(hk_z^t)} = Q. \quad (\text{S8.8})$$

$Q$  is an explicit expression containing  $k_z^l$  and  $k_z^t$ , and the elastic properties of the medium.

For the silicon membrane with Lamb wave propagation along the [110]-direction discussed in the main text, we used the free software suite *Dispersion Curve* (DC)<sup>17</sup> developed by A. Huber to trace the dispersion curves of the decoupled symmetric and antisymmetric Lamb modes (for details see also

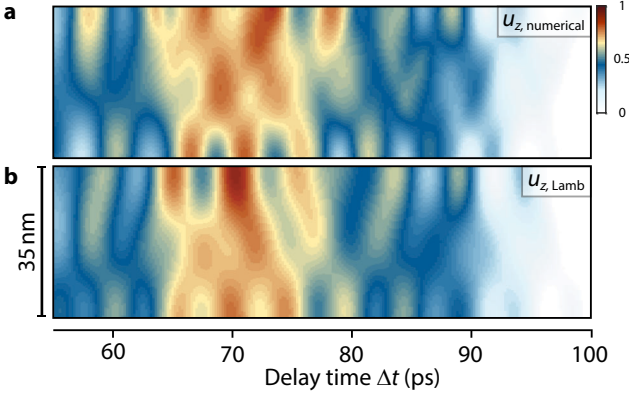


FIG. S3. Comparison of the numerically obtained displacement field (a) within the silicon membrane along the  $z$ -direction with corresponding results based on a Lamb wave superposition (b). Choosing a selection of Lamb modes at the specific resonance frequencies of the Pt/Si bilayer system [as indicated in Fig. 5(a)], the analytical superposition is in good agreement with the numerical results regarding spatial inhomogeneity and displacement oscillations.

Ref. 18). Dispersion curves for frequencies  $f$  up to 300 GHz and corresponding wavenumbers  $k$  up to  $0.4 \text{ nm}^{-1}$  are displayed in Fig. 4(a). It is confirmed that the expected limiting behavior<sup>12</sup> of the Lamb wave dispersion is recovered, such as

1. the cut-off frequency  $\times$  plate thickness products are equal to even or odd multiples of half of the sound velocities<sup>12</sup>  $v_l = 8433 \text{ m s}^{-1}$  and  $v_t = 5843 \text{ m s}^{-1}$ ,
2. phase velocities  $c_p = \frac{\omega}{k}$  of the  $A_0$  and  $S_0$  branch in the large- $k$  region approach the Rayleigh wave velocity  $v_R = v_t \cdot (0.718 - (v_t/v_l)^2)/(0.75 - (v_t/v_l)^2) = 5150 \text{ m s}^{-1}$  (approximation by Viktorov, Ref. 19),
3. the phase velocity of the  $S_0$  branch in the small- $k$  region<sup>20</sup> reaches  $\sqrt{(C_{11}^2 + C_{11}C_{12} - 2C_{12}^2 + 2C_{11}C_{44})/(2C_{11} \cdot \rho)} = 8533 \text{ m s}^{-1}$ .

For comparison of numerically solved displacement fields with a Lamb wave superposition, through-thickness profiles at the bilayer resonance frequencies were extracted from the DC software, considering all dispersion branches shown in Fig. 4(a). These profiles with individual propagation-induced phase terms are superimposed and the mean displacements extracted from the numerical simulations are added. Excluding the lowest-order 65.2 GHz resonance frequency, the dispersion field  $u_x$  in Fig. 5(b) is qualitatively in good agreement with the Lamb displacement superposition in Fig. 5(c) in the main text. Following the same procedure for  $u_z$ , a further simplification to only five displacement fields is possible, i.e., selecting the wavenumbers for frequencies 163.4 GHz on the  $A_0$ ,  $S_0$ ,  $A_1$ , and  $S_1$  branches and 208.0 GHz on  $A_0$ . The result is displayed in Fig. S3. We note that generally the Lamb wave dispersion depends on the static stress exerted on the membrane<sup>21</sup>, which could lead to small changes in the observed  $k/f$ -dependence.

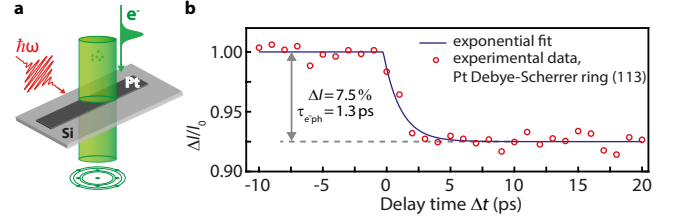


FIG. S4. Debye Waller analysis for the Pt/Si bilayer region. (a) Sketch of the experimental geometry for recording ultrafast parallel electron beam diffraction on the Pt/Si bilayer region. The diffraction pattern consists of a superposition of Bragg spots and Debye-Scherrer rings originating from silicon and platinum, respectively. (b) Delay-dependent intensity of the Pt (113) Debye-Scherrer ring after optical excitation. Adapting a single-exponential transient yields a platinum temperature increase of about 200 K. Within the first 20 ps, no subsequent temperature decrease is observed demonstrating that heat transfer to the underlying silicon membrane occurs on longer time scales.

## S9. DEBYE WALLER ANALYSIS

In order to extract the optically induced temperature rise of the 2- $\mu\text{m}$  wide polycrystalline platinum stripe on the silicon membrane, the decrease of the integrated diffraction intensity  $I$  in the Debye-Scherrer rings is acquired with a collimated electron beam (approx. 2.4- $\mu\text{m}$  spot diameter). For the (113)-ring, a total diffracted intensity change by 7.5% is observed at the same incident optical fluence as applied in the U-CBED experiment (see Fig. S4). To differentiate the temperature-dependent Bragg peak intensity and a broader diffuse background, we only consider a small scattering angle width around the (113)-ring for determining the diffracted intensity. The observed intensity drop corresponds to an optically induced increase of the lattice temperature from 300 K to about 506 K. Up to 70 ps after optical excitation, we did not observe a recovery of the ring intensity, in agreement with 500-ps-scale cooling time obtained numerically. The extracted effective electron-phonon coupling constant of 1.3 ps is in reasonable agreement with previous pump-probe experiments,<sup>22–24</sup> given the chosen delay steps of 1 ps and 700-fs electron pulse length. Furthermore, we confirmed that no irreversible structural changes occur up to an incident optical fluence of  $14 \text{ mJ cm}^{-2}$ .

- <sup>1</sup>A. Feist, N. Bach, N. Rubiano da Silva, T. Danz, M. Möller, K. E. Priebe, T. Domröse, J. G. Gatzmann, S. Rost, J. Schauss, S. Strauch, R. Bormann, M. Sivilis, S. Schäfer, and C. Ropers, “Ultrafast transmission electron microscopy using a laser-driven field emitter: Femtosecond resolution with a high coherence electron beam,” *Ultramicroscopy* **176**, 63–73 (2017).
- <sup>2</sup>J. R. Rumble, D. R. Lide, and T. J. Bruno, *CRC Handbook of Chemistry and Physics: A Ready-Reference Book of Chemical and Physical Data. 99th Edition.* (2018).
- <sup>3</sup>J. M. Cowley, *Diffraction Physics* (Elsevier, 1995).
- <sup>4</sup>J. M. Zuo and J. C. H. Spence, *Advanced Transmission Electron Microscopy: Imaging and Diffraction in Nanoscience* (Springer-Verlag, New York, 2017).
- <sup>5</sup>A. Morawiec, “Formal conditions for unambiguous residual strain determination by CBED,” *Philosophical Magazine* **85**, 1611–1623 (2005).
- <sup>6</sup>J. N. Clark, L. Beitra, G. Xiong, A. Higginbotham, D. M. Fritz, H. T. Lemke, D. Zhu, M. Chollet, G. J. Williams, M. Messerschmidt, B. Abbey, R. J. Harder, A. M. Korsunsky, J. S. Wark, and I. K. Robinson, “Ultrafast Three-Dimensional Imaging of Lattice Dynamics in Individual Gold Nanocrystals,” *Science* **341**, 56–59 (2013).
- <sup>7</sup>“COMSOL: Multiphysics Software for Optimizing Designs,” <https://www.comsol.com/>.
- <sup>8</sup>M. A. Hopcroft, W. D. Nix, and T. W. Kenny, “What is the Young’s Modulus of Silicon?” *Journal of Microelectromechanical Systems* **19**, 229–238 (2010).
- <sup>9</sup>A. F. Bower, *Applied Mechanics of Solids*, 1st ed. (Taylor & Francis Inc, Boca Raton, 2009).
- <sup>10</sup>W. S. M. Werner, K. Glantschnig, and C. Ambrosch-Draxl, “Optical Constants and Inelastic Electron-Scattering Data for 17 Elemental Metals,” *Journal of Physical and Chemical Reference Data* **38**, 1013–1092 (2009).
- <sup>11</sup>G. Hamaoui, N. Horny, Z. Hua, T. Zhu, J.-F. Robillard, A. Fleming, H. Ban, and M. Chirtoc, “Electronic contribution in heat transfer at metal-semiconductor and metal silicide-semiconductor interfaces,” *Scientific Reports* **8**, 11352 (2018).
- <sup>12</sup>D. Royer and E. Dieulesaint, *Elastic Waves in Solids* (Springer, Berlin; New York, 2000).
- <sup>13</sup>J. L. Rose, *Ultrasonic Guided Waves in Solid Media* (Cambridge University Press, Cambridge, 2014).
- <sup>14</sup>H. Lamb, “On waves in an elastic plate,” *Proceedings of the Royal Society of London. Series A, Containing Papers of a Mathematical and Physical Character* **93**, 114–128 (1917).
- <sup>15</sup>J. D. Achenbach, *Wave Propagation in Elastic Solids* (North Holland Pub. Co. ; American Elsevier Pub. Co., Amsterdam; New York, 1984).
- <sup>16</sup>Y. Li and R. B. Thompson, “Influence of anisotropy on the dispersion characteristics of guided ultrasonic plate modes,” *The Journal of the Acoustical Society of America* **87**, 1911–1931 (1990).
- <sup>17</sup>“Center for Lightweight-Production-Technology - The Dispersion Calculator: A free software for calculating dispersion curves of guided waves in multilayered composites,” [https://www.dlr.de/zlp/en/desktopdefault.aspx/tabid-14332/24874\\_read-61142/](https://www.dlr.de/zlp/en/desktopdefault.aspx/tabid-14332/24874_read-61142/).
- <sup>18</sup>A. Huber, “Numerical Modeling of Guided Waves in Anisotropic Composites with Application to Air-coupled Ultrasonic Inspection,” (2021).
- <sup>19</sup>I. A. Viktorov, *Rayleigh and Lamb Waves: Physical Theory and Applications* (Springer US, 1967).
- <sup>20</sup>S. V. Kuznetsov, “Low frequency limits for Lamb waves in homogeneous, stratified and functionally graded anisotropic plates,” *Mechanics of Advanced Materials and Structures* , 1–7 (2021).
- <sup>21</sup>B. Graczykowski, J. Gomis-Bresco, F. Alzina, J. S. Reparaz, A. Shchepetov, M. Prunnila, J. Ahopelto, and C. M. S. Torres, “Acoustic phonon propagation in ultra-thin Si membranes under biaxial stress field,” *New Journal of Physics* **16**, 073024 (2014).
- <sup>22</sup>A. P. Caffrey, P. E. Hopkins, J. M. Klopff, and P. M. Norris, “Thin Film Non-Noble Transition Metal Thermophysical Properties,” *Microscale Thermophysical Engineering* **9**, 365–377 (2005).
- <sup>23</sup>J. Hohlfeld, S. S. Wellershoff, J. Güdde, U. Conrad, V. Jähnke, and E. Matthias, “Electron and lattice dynamics following optical excitation of metals,” *Chemical Physics* **251**, 237–258 (2000).
- <sup>24</sup>D. Zahn, H. Seiler, Y. W. Windsor, and R. Ernstorfer, “Ultrafast lattice dynamics and electron–phonon coupling in platinum extracted with a global fitting approach for time-resolved polycrystalline diffraction data,” *Structural Dynamics* **8**, 064301 (2021).